



## Current assessment of integrated content of long-lived radionuclides in soils of the head part of the East Ural Radioactive Trace



I. Molchanova<sup>a</sup>, L. Mikhailovskaya<sup>a</sup>, K. Antonov<sup>b</sup>, V. Pozolotina<sup>c</sup>, E. Antonova<sup>c,\*</sup>

<sup>a</sup> Laboratory of Common Radioecology, Institute of Plant & Animal Ecology, Ural Branch of the Russian Academy of Sciences, 202 8 Marta St., 620144 Ekaterinburg, Russian Federation

<sup>b</sup> Laboratory of Territories Sustainable Development, Institute of Industrial Ecology, Ural Branch of the Russian Academy of Sciences, 20 Kovalevskoy St., 620990 Ekaterinburg, Russian Federation

<sup>c</sup> Laboratory of Population Radiobiology, Institute of Plant & Animal Ecology, Ural Branch of the Russian Academy of Sciences, 202 8 Marta St., 620144 Ekaterinburg, Russian Federation

### ARTICLE INFO

#### Article history:

Received 20 November 2013

Received in revised form

30 June 2014

Accepted 5 September 2014

Available online

#### Keywords:

Kyshtym accident

East Ural Radioactive Trace (EURT)

Artificial radionuclides

Integrated content

Ordinary kriging

Monte Carlo methods

### ABSTRACT

Based on the datasets obtained during investigations from 2003 to 2012, the spatial distributions of <sup>90</sup>Sr, <sup>137</sup>Cs, and <sup>239,240</sup>Pu content in the soils of the head part of the East Ural Radioactive Trace (EURT) were mapped using the geographic information system ArcGIS. Taking into account the presence of spatial autocorrelation and anisotropy in the source data, an ordinary kriging method was applied to interpolate values of radionuclide contamination density at unsampled places. Further geostatistical data analysis was performed to determine the basic parameters of spatial dependencies and to integrally assess the contamination by long-lived radionuclides in soils of the central, east peripheral, and west peripheral parts of the trace. This analysis was based on simplified geometric models (sector- and rectangle-shaped areas). The Monte Carlo method was used to quantitatively assess the uncertainty of the values for the integrated quantities resulting from the statistical errors of the source data approximation.

© 2014 Elsevier Ltd. All rights reserved.

### 1. Introduction

The East Ural Radioactive Trace (EURT) is a result of the accident at the Production Association (PA) Mayak in 1957 (the so-called Kyshtym accident). Among the long-lived radionuclides, <sup>90</sup>Sr was the primary emission contaminant at the time of the accident. The most significant concentration of <sup>90</sup>Sr was in the north-east zone, near the accident epicenter (a narrow sector of approx. 15°, 35 km long). Later, in 1967, the EURT area was contaminated again with air-borne radioactive sediments from the shores of Lake Karachay, which was used by the PA Mayak for dumping liquid radioactive waste. In this case the primary contaminant was <sup>137</sup>Cs, most of which was spread within a 60° sector oriented in the same direction (Aarkrog et al., 1997; Romanov et al., 1990; Tsaturov and Anisimova, 1993). In 1966, the East Ural State Reserve (EUSR) with a total area of 166 km<sup>2</sup>

was established next to the epicenter. In the following years, many studies were conducted in the area aiming to achieve a greater understanding of migration for the key contaminants in the soil-plant cover and the long-term dynamics of the radiation situation at the EURT (Chukanov et al., 1996; Pozolotina et al., 2008, 2012; Sokolov and Krivolutsky, 1993).

Earlier radioecological studies included the assessment of integrated quantities of <sup>90</sup>Sr, <sup>137</sup>Cs, and <sup>239,240</sup>Pu only within the central axis of the trace (Molchanova et al., 2009). The database on soil contamination, continuously updated over the last 10 years, enables an estimation of the current radionuclide contents not only in the zone with the highest contamination levels (the central axis) but also in adjacent areas. Data on spatial distribution of radionuclides should be considered when assessing the possibility for economic use of lands or radiation exposure of living organisms (Brown et al., 2008; Karimullina et al., 2013).

Powerful tools for up-to-date radioecological and ecotoxicological investigations include the geographic information systems implemented in various software (e.g. ArcGIS, EDSS, PRANA, Surfer, MapGIS, geoR, etc.). These systems are being widely used for modeling the spatial pattern of contaminants in different environmental components as well as for identifying sources of

\* Corresponding author. Tel.: +7 343 260 82 55; fax: +7 343 260 65 00.

E-mail addresses: [selena@ipae.uran.ru](mailto:selena@ipae.uran.ru), [elena.v.antonova79@gmail.com](mailto:elena.v.antonova79@gmail.com) (E. Antonova).

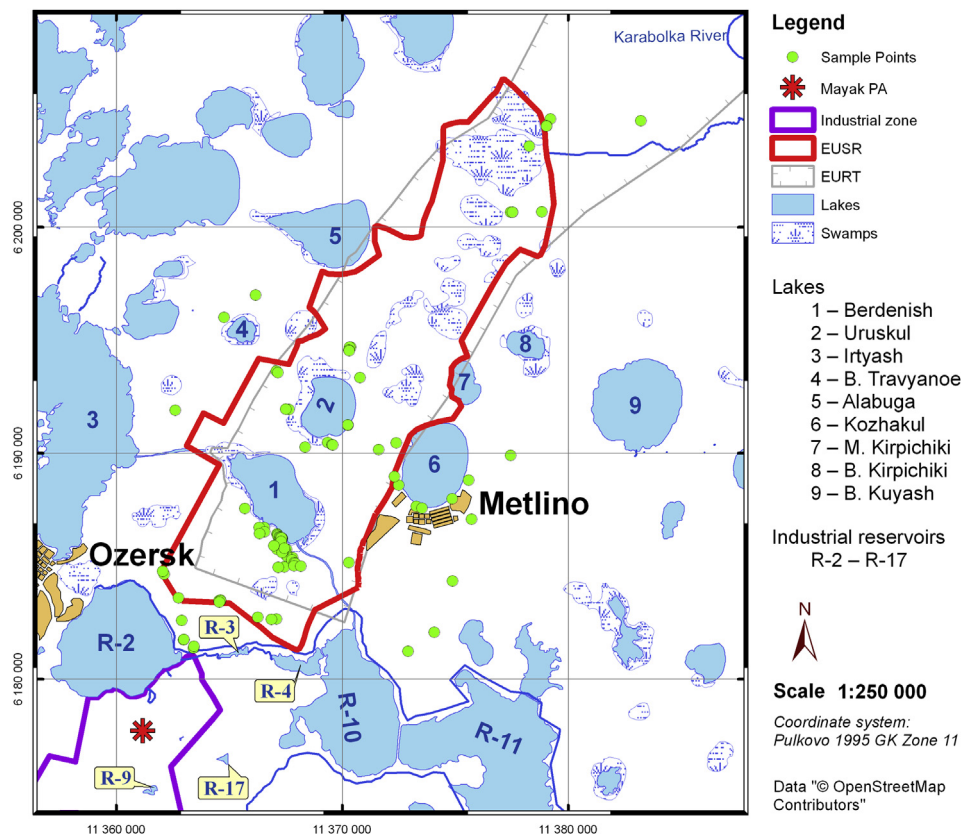


Fig. 1. Study area map.

pollution, estimating radionuclide migration, calculation of radiation doses and ecological risk assessments (Van der Perk et al., 2000; Yatsalo et al., 2000; Facchinelli et al., 2001; Mabit and Bernard, 2007; Zhao et al., 2012; Caro et al., 2013; Hejl et al., 2013).

This research was aimed at characterizing and quantifying the current contamination levels for  $^{90}\text{Sr}$ ,  $^{137}\text{Cs}$ , and  $^{239,240}\text{Pu}$  in soils near the accident epicenter of the EURT (within 0–35 km) and to provide detailed baseline data for the activity density and spatial distribution patterns in surface soil using advanced geostatistical models embedded in ArcGIS software (ESRI, 2009).

## 2. Materials and methods

### 2.1. The study sites

The territories studied are in the EUTR, located within the Trans-Ural forest-steppe that is characterized by alternating steppe meadows, birch forests, small groves of mixed birch and aspen and pine forests. The relief is hilly with the entire area sloping down from west to east. The soil types are dominated with various subtypes of forest gray soils, meadow soils and chernozem soils of varying thickness and degree of leaching (Pozolotina et al., 2012). Westerly and southwesterly winds prevailing in the region determined the shape of the trace (Teterin, 2011).

### 2.2. Sampling method

The studied area of the head part of the trace was graded according to the levels of radionuclides present. The impact zone within the central axis of the trace covered an area approximately 4 km wide and 35 km long. Buffer zones adjacent to the east and west sides of the impact zone, both 6–8 km wide, were considered

the trace periphery, where the gradient of radionuclide contamination falls to the background level. Soil samples were taken in all zones in the period from 2003 to 2012. Sampling was done at different distances from the accident epicenter. Since a considerable part of the EURT area is covered by lakes and impassable marshlands, sampling locations were distributed in space neither evenly nor randomly; they demonstrate a high degree of clusterization (Fig. 1). In order to assess the spatial distribution of radionuclides in the peripheral locations, soil samples were obtained from across the entire breadth of the contaminated area. Two parallel imaginary transects were laid down to make this possible. One transect was positioned at 6–8 km and another – at 16–18 km away from the accident epicenter. Sampling locations at the west and east peripheral areas were positioned at equal distances from the central axis of the trace, at approx. 5–6 km.

Soil profile cuts were positioned at the selected locations. Samples were taken in 5–10 cm layers down to a depth of 25–50 cm. The total content of radionuclides in the investigated layer of soil per unit of area was stipulated to be referred to as the *content* or radionuclide contamination *density*.

### 2.3. Methods for determination of radionuclides

All of the samples were air dried and then ashed at  $t = 450^\circ\text{C}$ . The technique for radiochemical determination of  $^{90}\text{Sr}$  in environmental samples is based on applying stable Sr as an isotope carrier then leaching with 6N hydrochloric acid. Then Sr oxalate forms were precipitated and the daughter  $^{90}\text{Y}$  was separated from  $^{90}\text{Sr}$  with the use of mono-isooctyl ester of methylphosphonic acid. This combination forms insoluble complexes with stable Fe and  $^{90}\text{Y}$ . Finally, the yield of stable carrier was determined using the method described by Tsvetaeva et al. (1984). Radiometric measurements of

resulting specimens were carried out on a low background  $\alpha$ - $\beta$ -radiometer with a siliceous detector. The minimum detection limit was 0.2 Bq.

The content of  $^{137}\text{Cs}$  in the samples was determined using a gamma-spectrometer with a germanium detector. The gamma spectra were collected employing a Canberra-1510 multichannel analyzer and GENIE-PC software (Canberra-Packard, USA). Minimum detection level for this spectrometer was 0.1 Bq.

The analytical determination of the  $^{239,240}\text{Pu}$  content included applying  $^{242}\text{Pu}$  as a marker, leaching by a mix of strong acids ( $\text{HNO}_3 + \text{HCl}$ ), cleaning the solution on ion-exchange resins and then electrolytic deposition (Chen et al., 1993). The alpha activity of the samples was studied using an  $\alpha$ -spectrometer ALPHA-ANALYST equipped with a PIPS detector (Canberra-Packard, USA). The  $\alpha$ -spectra were analyzed with GENIE-2000 software. The minimum detection level was 0.001 Bq. In some cases the plutonium content in averaged soil samples was determined without splitting them over soil layers.

The minimum detection level mentioned above corresponded to the specifications of the spectrometers. All of the measurements performed in the framework of this research followed the ISO/IEC 17025 (2005) requirements. An error for analysis of  $^{137}\text{Cs}$  by  $\gamma$ -spectrometer included the sum of errors during sample preparation and errors coming from the analytical technique. An error for radiochemical analysis of  $^{90}\text{Sr}$  included, in addition, an error for determination of isotope carrier. The determination of Pu also included an error of  $\alpha$ -spectroscopic determination of the marker activity ( $^{242}\text{Pu}$ ). The inaccuracy of radionuclide determination methods does not exceed 20%. All of the determination results were corrected for radionuclide decay to the time of calculations (2012).

#### 2.4. Mapping procedures and construction of geostatistical models

Mapping the radio-contaminant activity density or activity concentration is a useful method for better understanding the spatial distribution pattern of radionuclides. In this study all data-sets of radionuclide soil contaminations were employed to create prediction maps using an advanced geostatistical method – the interpolation technique of ordinary kriging (Webster and Oliver, 2007). Since the locations of the soil sampling were clustered and the radionuclide content was highly variable within relatively small areas, the traditional deterministic interpolation techniques for the construction of spatial contamination maps such as inverse distance weighting (IDW) or radial basis function (RBF) methods could not be adapted satisfactory. As Mabit and Bernard (2007) demonstrated, these methods set aside the existing spatial structure (autocorrelation) of data and thus oversimplify reality during spatial modeling of radionuclide contamination. In addition, they are far too sensitive to the initial conditions and they yield results that are difficult to interpret due to manifestations of the “bull’s eye” effect.

Creating a surface with geostatistical methods, including ordinary kriging, involves (a) exploratory and (b) structural analysis (Johnston et al., 2001). In the first case, the normality of univariate distributions (histogram and quantile–quantile plotting) is examined for assigning the possible way of initial data transformation. Then the spatial trend analysis is applied to decompose transformed data into a deterministic trend component and an autocorrelated random component of the spatial distribution patterns. The trends should be removed from the further analysis of the sampled points (so-called process of detrending) but added back in before predictions are made. All mentioned procedures need to be performed in order to satisfy key geostatistics assumptions, viz. the stationarity hypothesis. Stationarity implies that the distribution of the random process has certain attributes that only depend on the

distance between points and not on absolute positions (Webster and Oliver, 2007). In fact, this condition is very restrictive and seldom achieved in environmental studies, but it is a mandatory consideration when geostatistics are being used (Dubois and Bossew, 2003; Caro et al., 2013).

In case (b), the analysis aims at a quantitative assessment of spatial autocorrelation, quantifying the assumption that samples close together in space are more alike than those farther apart. This is known as variography – fitting a spatial-dependence variogram model for the best approximation of the empirical variance (semivariance) of pairs of observations (data points) at increasing distance between these observations and in several directions (Webster and Oliver, 2007). In this task, the exponential variogram has proven to be the most adequate to fit the spatial dependence among the transformed data,

$$2g(h) = C_0 + C_1(1 - \exp\{-3h/R\})$$

where  $g(h)$  is the theoretical semivariogram;  $h$  is the distance between data points;  $C_0$  is the nugget variance;  $C_1$  is the partial sill; and  $R$  is the range parameter.

The nugget effect,  $C_0$ , describes the small-scale spatial variation produced by various sources of uncertainty (e.g. measurement error, sampling error, unexplained and inherent variability) when  $h = 0$  (at scales shorter than the distances between neighboring sites). The sill,  $C_0 + C_1$ , corresponds to the model asymptote (partial sill and the nugget effect) and should be equal to the variance of the data set. The range,  $R$ , is the distance at which the difference between the variogram from the sill becomes negligible (less than 5%), and thereby represents the separation distance over which no more spatial correlation is apparent. The ratio of nugget variance to sill variance (“nugget-to-sill” ratio, %) can be used to estimate the spatial dependence strength (Mabit and Bernard, 2007; Caro et al., 2013). If the ratio is less than 25%, the variable has a strong spatial dependence. Between 25% and 75%, the spatial dependence is considered as moderate, and if the ratio exceeds 75% the variable shows only weak spatial autocorrelation.

When modeling a variogram, directional dependence in the spatial autocorrelation, which is called anisotropy, has to be tested. As opposed to trends, anisotropy is usually not a deterministic process with an unknown cause; so it is modeled as a random error. To identify and estimate anisotropy, transects must be aligned in some directions. If the variogram gradients or ranges markedly differ along different transects, then it is likely that the underlying variation is anisotropic (Webster and Oliver, 2007). In this work, major ranges,  $R_1$ , and minor ranges,  $R_2$ , were determined in the orthogonal axes. Therefore, the ratio  $R_1/R_2$  (anisotropy factor) quantifying anisotropy should be taken into account when mapping.

Hereby, the information generated through variogram construction describes the spatial autocorrelation as well as the input parameters for kriging interpolation. Optimally fitted parameters, including anisotropy, allow for building a more adequate (smoother) image of radionuclide contamination over a given area. For evaluating the optimal parameters and examining the prediction performances of the interpolation models, cross-validation analysis was used. This involves the construction of the linear regression between the predicted and observed (actual) values of radionuclide content. For an acceptable cross-validation, the regression coefficient (the slope of the regression) needs to be as close as possible to 1. In the case of a spatial structure,  $R^2$  value (proportion of variation explained by the regression) should be greater than 0.2 (Mabit and Bernard, 2007). All the above-mentioned geostatistical methods and techniques were implemented within the Geostatistical Analyst module of the ArcGIS 9.3

**Table 1**  
Radionuclides in soil at the trace central axis at 4 km from the accident epicenter (55°44' N, 60°49' E).

Depth, cm	<sup>90</sup> Sr		<sup>137</sup> Cs		<sup>239,240</sup> Pu	
	kBq kg <sup>-1</sup>	kBq m <sup>-2</sup>	kBq kg <sup>-1</sup>	kBq m <sup>-2</sup>	kBq kg <sup>-1</sup>	kBq m <sup>-2</sup>
Forest litter	139.2 ± 14.3	69.6 ± 7.1	1.6 ± 0.07	0.8 ± 0.04	Not detected	
0–5	147.0 ± 0.1	7056 ± 4.8	5.2 ± 0.6	251.7 ± 29.0	0.49 ± 0.06	23.6 ± 2.9
5–10	163.0 ± 0.6	8802 ± 32.4	5.5 ± 0.6	296.8 ± 32.4	0.54 ± 0.07	29.2 ± 3.8
10–15	250.2 ± 0.8	17,514 ± 56.0	6.0 ± 0.7	421.7 ± 49.2	0.78 ± 0.09	54.9 ± 6.3
15–20	269.1 ± 0.8	17,220 ± 56.0	5.3 ± 0.6	341.4 ± 38.6	0.82 ± 0.10	52.7 ± 6.4
20–30	148.9 ± 0.6	15,824 ± 63.8	1.9 ± 0.2	199.4 ± 21.0	0.43 ± 0.06	46.3 ± 6.5
30–40	23.4 ± 0.3	2313 ± 29.7	0.06 ± 0.005	5.7 ± 0.5	0.06 ± 0.009	6.3 ± 0.9
40–50	1.5 ± 0.1	201 ± 13.4	0.006 ± 0.001	0.8 ± 0.1	0.004 ± 0.0008	0.5 ± 0.1
Content		69,073.8		1518.4		213.5

software (ESRI, 2009). It is to be emphasized that ordinary kriging only was applied for visualizing the values of soil activity at unsampled places in order to obtain a qualitative spatial pattern of radionuclide contamination of the head part of the EURT rather than a detailed quantitative assessment of the radionuclide budget.

For the calculations of the integrated contents of <sup>90</sup>Sr, <sup>137</sup>Cs, and <sup>239,240</sup>Pu within the trace central axis and the adjacent areas, simple geometric models (sector- and rectangle-shaped areas) were used, with roughly north-east oriented distances from the epicenter not exceeding 35 km. When determining the sector boundaries, the existing literature data was summarized (Aarkrog et al., 1998; Romanov et al., 1990; Tsaturov and Anisimova, 1993). Rectangle models were suggested within this research. The modeled areas completely cover the head part of the EURT where 70% of the studied radionuclide activity is concentrated due to the fallouts of the accidents described the Introduction (Molchanova et al., 2009). Then, the functions of the radionuclides' spatial distributions within each model were set empirically. Finally, the function parameters served as a basis for the integrated quantities assessment.

The uncertainties of integrated assessments were computed with the Monte Carlo method, often called the statistical tests method (Hammersley and Handscomb, 1964; Rubinstein and Kroese, 2008). In the present work, it implies the numerical simulation of the arguments of radionuclides' spatial distribution functions based on the empirically obtained randomness parameters (means and standard errors) of these arguments. For each case, 10,000 values were generated, which were then used for modeling the univariate distribution of an integrated radionuclide quantity and determining the 95% confidence interval of its point assessment.

Routine statistical analysis, namely the statistical assessment of univariate distributions via the Kolmogorov–Smirnov test as well as the estimation of linear regression model parameters, their standard error values, and the  $R^2$  determination coefficients, was performed under the basic and regression modules of Statistica 6.0 software (StatSoft Inc., 2001).

### 3. Results

An inventory of the existing data (38 sampling locations) was performed in 2009 that was documented by Molchanova et al. that same year. Currently, the database includes information on 102 soil profile cuts. Some of the newly obtained data are presented below. Apart from the data on contamination density (kBq m<sup>-2</sup>), the tables include data on the activity of the soils (kBq kg<sup>-1</sup>) that might be required for the calculation of doses to non-human biota.

#### 3.1. Trace central axis radionuclide content

At the southern border of the EURT, 4 km from the location of the accident, areas have been found to contain quantities of <sup>90</sup>Sr in

soils up to 69074 kBq m<sup>-2</sup>, <sup>137</sup>Cs reaching 1518 kBq m<sup>-2</sup>, and <sup>239,240</sup>Pu reaching 214 kBq m<sup>-2</sup> (Table 1). At 20 km from the contamination epicenter, the radionuclide quantities were about ten times lower (Table 2), and at 35 km – about a hundred times lower (Table 3).

The new data fits well into the suggested earlier exponential curve describing the decrease of the contamination levels with increasing distance from the accident epicenter (Molchanova et al., 2009). It is evident that radionuclide contamination densities within the trace central axis significantly exceeds the background radiation levels that for the Ural region are as follows: 0.3–3.0 kBq m<sup>-2</sup> for <sup>90</sup>Sr, 1.0–6.0 kBq m<sup>-2</sup> for <sup>137</sup>Cs, and 0.02–0.3 kBq m<sup>-2</sup> for <sup>239,240</sup>Pu (Laverov, 2007; Mikhailovskaia et al., 2011). It should be noted that most of the radionuclide content is concentrated in the 0–30 cm layer in the immediate vicinity of the contamination source. The thickness of the contaminated layer decreases as the distance from the accident epicenter grows.

#### 3.2. Buffer territories radionuclide content

The soil test results of the peripheral areas at 6–8 km from the accident epicenter (the first transect) are presented in Tables 4 and 5. The content of radionuclides in soil of the west peripheral area is two to five times lower than that in the east peripheral area. Similar results were obtained for the transect positioned at 16–18 km from the epicenter (Tables 6 and 7). Earlier results also demonstrated higher contamination levels in the eastern parts within the areas adjacent to the impact zone (Molchanova et al., 2009).

#### 3.3. Variability of radionuclide content at areas in close proximity

It is important to point out that areas relatively close to each other, in similar topological and ecological conditions, may differ up to one order of magnitude in terms of their estimated radionuclide content. For instance, the <sup>90</sup>Sr content varies from 1200 kBq m<sup>-2</sup> to 33400 kBq m<sup>-2</sup>, <sup>137</sup>Cs – from 66 to 646 kBq m<sup>-2</sup>, and <sup>239,240</sup>Pu from 2.2 to 92 kBq m<sup>-2</sup> at a limited dry meadow area (100 m<sup>2</sup>) located within the central axis 13 km away from the accident epicenter. The variability of <sup>90</sup>Sr is higher than that of <sup>137</sup>Cs and <sup>239,240</sup>Pu as is evident from the coefficients of variation calculated on the basis of the existing data (Table 8). Variability of the <sup>90</sup>Sr contamination density also reaches its highest values in the east peripheral area of the trace. This confirms the earlier data which suggested a mosaic pattern structure of radioactive fallout (Bakurov et al., 2007).

#### 3.4. Spatial distribution of radionuclides

The entirety of the existing data on the density of soil contamination by <sup>90</sup>Sr, <sup>137</sup>Cs, and <sup>239,240</sup>Pu (102 sampling locations) was

**Table 2**  
Radionuclides in soil at the trace central axis at 20 km from the accident epicenter (55°51'N, 60°55' E).

Depth, cm	<sup>90</sup> Sr		<sup>137</sup> Cs		<sup>239,240</sup> Pu	
	kBq kg <sup>-1</sup>	kBq m <sup>-2</sup>	kBq kg <sup>-1</sup>	kBq m <sup>-2</sup>	kBq kg <sup>-1</sup>	kBq m <sup>-2</sup>
0–5	16.2 ± 1.8	663 ± 73.7	1.0 ± 0.05	39.5 ± 1.9	0.06 ± 0.006	2.5 ± 0.2
5–10	22.3 ± 2.4	1519 ± 163.4	1.0 ± 0.05	69.9 ± 3.5	0.08 ± 0.008	5.4 ± 0.5
10–15	30.5 ± 3.2	2502 ± 262.5	1.2 ± 0.05	100.4 ± 5.0	0.10 ± 0.01	8.6 ± 0.9
15–20	34.4 ± 0.3	2544 ± 22.2	0.7 ± 0.04	54.6 ± 3.1	0.11 ± 0.006	7.9 ± 0.5
20–30	8.5 ± 0.2	1437 ± 33.8	0.08 ± 0.005	12.9 ± 0.8	0.02 ± 0.003	4.1 ± 0.6
30–40	1.5 ± 0.08	189.4 ± 10.1	0.01 ± 0.001	1.3 ± 0.1	0.004 ± 0.001	0.5 ± 0.1
40–50	0.4 ± 0.07	14.6 ± 2.6	0.01 ± 0.002	0.4 ± 0.08	0.001 ± 0.0002	0.04 ± 0.008
Content		8878.7		279.0		29.0

**Table 3**  
Radionuclides in soil at the trace central axis at 35 km from the accident epicenter (55°56' N, 61°03' E).

Depth, cm	<sup>90</sup> Sr		<sup>137</sup> Cs		<sup>239,240</sup> Pu	
	kBq kg <sup>-1</sup>	kBq m <sup>-2</sup>	kBq kg <sup>-1</sup>	kBq m <sup>-2</sup>	kBq kg <sup>-1</sup>	kBq m <sup>-2</sup>
0–5	2.7 ± 0.3	106.4 ± 10.6	0.3 ± 0.02	12.9 ± 0.7	0.01 ± 0.003	0.5 ± 0.1
5–10	2.1 ± 0.2	157.4 ± 15.7	0.3 ± 0.02	18.8 ± 0.9	0.01 ± 0.003	0.7 ± 0.2
10–15	1.5 ± 0.2	109.3 ± 10.9	0.08 ± 0.004	5.5 ± 0.3	0.005 ± 0.001	0.4 ± 0.1
15–20	0.9 ± 0.09	54.2 ± 5.4	0.04 ± 0.004	2.2 ± 0.1	0.003 ± 0.001	0.2 ± 0.05
20–25	0.4 ± 0.04	26.2 ± 2.6	0.009 ± 0.001	0.5 ± 0.03	0.001 ± 0.0003	0.08 ± 0.02
25–30	0.2 ± 0.02	14.4 ± 1.4	0.004 ± 0.0004	0.2 ± 0.01	0.001 ± 0.0003	0.04 ± 0.01
30–40	0.5 ± 0.05	77.3 ± 7.7	0.01 ± 0.0005	1.9 ± 0.1	0.002 ± 0.0003	0.2 ± 0.05
Content		496.1		42.0		2.12

used for mapping the radionuclide contamination across the study area. The exploratory and structural analysis of the data revealed a number of spatial distribution characteristics that are crucial for the ordinary kriging method and determine – to a considerable degree – the shape of the surfaces being interpolated.

Firstly, the empirical univariate distributions of the activity density for all radionuclides appeared to be abnormal (Fig. 2, left column); its skewness and kurtosis are significantly higher than zero (for <sup>137</sup>Cs as minimum values with 2 × S.E.: 1.86 ± 0.48 and 3.12 ± 0.94, respectively). This means that the explored sample distributions have a strong positive asymmetric nature with right-hand tail, i.e. the majority of samples presented with relatively low values (for instance <sup>90</sup>Sr – from 3 to 5000 kBq m<sup>-2</sup> with maximum value of about 70000 kBq m<sup>-2</sup>). Generally, “right-hand tail” asymptotics of the empirical distributions of the activity density and activity concentration are often typical of spatial patterns of radionuclide deposition. Such a case was demonstrated for soil contamination by the Chernobyl and Fukushima fallouts (Dubois and Bossew, 2003; Grubich et al., 2013).

Although normality may not be strictly required, a serious violation of normality, such as excessively high skewness and outliers, can impair the variogram structure and the kriging results (Johnston et al., 2001). Sample distributions were described

appropriately by log-normal function in accordance with the Kolmogorov–Smirnov test. Since *d*-statistics were not statistically significant in all of the cases (*p* < 0.2), log-normal distribution is only an approximate statistical model of radionuclides' univariate pattern that assigns the possible way of initial data transformation – taking the logarithm. For the data transformed in this way, the values of skewness and kurtosis do not differ significantly from zero (for all radionuclides, the skewness varies from –0.65 ± 0.52 to –0.29 ± 0.48, kurtosis from –0.27 ± 0.94 to –0.22 ± 0.94).

Secondly, when moving away from the epicenter, in all cases the logarithmic data presented deterministic components of soil contamination that are optimally approximated by linear trends (see right column on Fig. 2). These contamination gradients are obviously related to the EURT formation that resulted from the Kyshtym and Karachay accidents as well as scheduled emissions from the PA Mayak facilities. Linear trend values were subtracted from the converted data before the structural analysis and then were added back to the output surfaces before the final interpolation.

Thirdly, at the structural analysis stage, the spatial autocorrelation of the detrended log data of the radionuclide contamination density was estimated through exponential variogram models, being the most adequate to the solving interpolation task.

**Table 4**  
Radionuclides in soil at the west peripheral area of the trace at 6–8 km from the accident epicenter (55°45' N, 60°48' E).

Depth, cm	<sup>90</sup> Sr		<sup>137</sup> Cs		<sup>239,240</sup> Pu
	kBq kg <sup>-1</sup>	kBq m <sup>-2</sup>	kBq kg <sup>-1</sup>	kBq m <sup>-2</sup>	kBq m <sup>-2</sup>
Forest litter	2.4 ± 1.7	4.2 ± 0.7	0.7 ± 0.3	2.4 ± 1.0	
0–5	1.0 ± 0.8	16.8 ± 5.0	0.3 ± 0.1	13.5 ± 4.5	
5–10	0.13 ± 0.06	31.8 ± 15.0	0.09 ± 0.04	6.0 ± 3.0	
10–15	0.07 ± 0.03	20.8 ± 8.0	0.03 ± 0.01	1.8 ± 0.6	
15–20	0.06 ± 0.03	3.3 ± 1.2	0.03 ± 0.01	2.1 ± 0.7	
20–25	0.01 ± 0.005	1.2 ± 0.5	0.03 ± 0.01	2.4 ± 0.8	
25–30	0.02 ± 0.005	1.4 ± 0.7	0.02 ± 0.01	1.2 ± 0.6	
Content		79.5		29.4	0.8 <sup>a</sup>

<sup>a</sup> Plutonium isotopes quantities were not determined for each layer individually.

**Table 5**  
Radionuclides in soil at the east peripheral area of the trace at 6–8 km from the accident epicenter (55°44' N, 60°52' E).

Depth, cm	<sup>90</sup> Sr		<sup>137</sup> Cs		<sup>239,240</sup> Pu
	kBq kg <sup>-1</sup>	kBq m <sup>-2</sup>	kBq kg <sup>-1</sup>	kBq m <sup>-2</sup>	kBq m <sup>-2</sup>
Forest litter	1.3 ± 0.8	1.4 ± 0.9	0.3 ± 0.2	0.3 ± 0.2	
0–5	1.3 ± 1.0	18.6 ± 10.4	4.8 ± 4.6	56.8 ± 25.9	
5–10	1.5 ± 1.0	69.7 ± 46.2	0.8 ± 0.4	36.8 ± 21.3	
10–15	0.2 ± 0.1	14.2 ± 7.0	0.1 ± 0.08	5.9 ± 4.0	
15–20	0.2 ± 0.1	12.5 ± 6.0	0.02 ± 0.01	1.6 ± 0.8	
20–25	0.05 ± 0.001	2.4 ± 0.6	0.007 ± 0.003	0.4 ± 0.1	
25–30	0.1 ± 0.005	7.0 ± 0.3	0.009 ± 0.003	0.6 ± 0.2	
Content		125.8		102.4	3.3 <sup>a</sup>

<sup>a</sup> Plutonium isotopes quantities were not determined for each layer individually.

**Table 6**

Radionuclides in soil at the west peripheral area of the trace at 16–18 km from the accident epicenter (55° 52' N, 60° 50' E).

Depth	<sup>90</sup> Sr		<sup>137</sup> Cs		<sup>239,240</sup> Pu	
	kBq kg <sup>-1</sup>	kBq m <sup>-2</sup>	kBq kg <sup>-1</sup>	kBq m <sup>-2</sup>	kBq kg <sup>-1</sup>	kBq m <sup>-2</sup>
Forest litter	0.6 ± 0.2	0.8 ± 0.2	0.02 ± 0.008	0.02 ± 0.005	0.002 ± 0.001	0.003 ± 0.002
0–5	0.1 ± 0.02	2.1 ± 0.4	0.12 ± 0.05	3.4 ± 1.3	0.01 ± 0.001	0.3 ± 0.1
5–10	0.09 ± 0.03	4.2 ± 0.9	0.03 ± 0.008	1.1 ± 0.3	0.004 ± 0.001	0.15 ± 0.05
10–15	0.08 ± 0.02	3.7 ± 1.0	0.023 ± 0.008	0.9 ± 0.3	0.003 ± 0.001	0.15 ± 0.05
15–20	0.04 ± 0.01	2.6 ± 0.5	0.01 ± 0.002	0.9 ± 0.3	–	–
20–25	0.02 ± 0.005	0.6 ± 0.2	0.005 ± 0.001	0.2 ± 0.1	–	–
Content		14.0		6.5		0.6

**Table 7**

Radionuclides in soil at the east peripheral area of the trace at 16–18 km from the accident epicenter (55° 48' N, 61° 00' E).

Depth, cm	<sup>90</sup> Sr		<sup>137</sup> Cs		<sup>239,240</sup> Pu	
	kBq kg <sup>-1</sup>	kBq m <sup>-2</sup>	kBq kg <sup>-1</sup>	kBq m <sup>-2</sup>	kBq kg <sup>-1</sup>	kBq m <sup>-2</sup>
Forest litter	0.9 ± 0.5	0.6 ± 0.2	0.4 ± 0.3	0.6 ± 0.3	0.001 ± 0.0005	0.001 ± 0.0005
0–5	0.3 ± 0.08	9.6 ± 5.6	0.6 ± 0.3	22.3 ± 19.6	0.008 ± 0.003	0.3 ± 0.1
5–10	0.2 ± 0.08	7.1 ± 2.1	0.3 ± 0.1	10.7 ± 1.9	0.002 ± 0.0008	0.1 ± 0.03
10–20	0.1 ± 0.02	6.9 ± 2.1	0.5 ± 0.1	10.7 ± 1.1	0.001 ± 0.0004	0.1 ± 0.03
20–30	0.008 ± 0.002	1.3 ± 0.1	Not determined	–	–	–
Content		25.5		44.3		0.5

Variogram parameters that are at the same time the input parameters for the kriging method were fitted in the auto calculation mode of the ArcGIS system with the mandatory “anisotropy option” switched on. The results for all of the considered radionuclides are summarized in Table 9.

The transformed data for all of the radionuclides revealed moderate spatial dependence; the “nugget-to-sill” ratios range within 44–64%. Furthermore, the dependencies of autocorrelation on the direction were detected explicitly due to significant differences between the variograms' major and minor ranges. The calculated anisotropy factors vary within 1.8–6.2 with the main axis directed to roughly north-east bearing 18°–26°. In these conditions, mapping strategy to visualize studied radionuclides contamination appeared to be more adequate with ordinary kriging rather than classical methods of interpolation (IDW, RBF, etc.). Furthermore, the cross-validation analysis showed that ordinary kriging models with mentioned options provided acceptable  $R^2$  values of 0.53 for <sup>90</sup>Sr, 0.68 for <sup>137</sup>Cs and 0.52 for <sup>239,240</sup>Pu. The regression coefficients (1.48, 0.70 and 0.82 for the same radionuclides, respectively) also denoted the satisfactory goodness of fit for the applied models. For strontium, it slightly overestimates the larger values and underestimates the smaller ones and for cesium and plutonium vice versa. All other interpolation methods tested in this research yielded less significant results of the cross-validation procedures. The results of interpolation within the head part of the EURT and the adjacent areas are presented in Fig. 3 (a, b, c). Note that the second-order stationarity hypothesis was not verified.

It is clear from Fig. 3 that all the radionuclide content mapping which applied the ordinary kriging method matches the grading of the study area performed earlier (Molchanova et al., 2009). The central axis (2–4 km wide) is the most contaminated area. The

radionuclide contents decrease rapidly as the distance from the epicenter of the accident increases. The contents of all radionuclides decrease 30–100 times on average. In the peripheral areas the density gradients vary insignificantly, regardless of the distance to the epicenter. This fact is in good agreement with the results of other studies of the central axis (Raputa, 2006) and the EURT in whole (Vasilenko et al., 1998; Volobuev et al., 2004; Laverov, 2007).

### 3.5. Assessment of integrated content of radionuclides

Simplified geometric models, viz. sectors and rectangles, were used for the assessment of integrated quantities of radionuclides within the delineated areas (central, west, and east). When determining the sector boundaries, the existing literature data was consolidated (Aarkrog et al., 1998; Romanov et al., 1990; Tsaturov and Anisimova, 1993). These data indicated that activities of <sup>90</sup>Sr from the Kyshtym accident and <sup>137</sup>Cs from the Karachay accident were concentrated within the 15° and 60° sectors, respectively. Based on the existing data an aggregate 60° sector with a 4 km–35 km radius was constructed covering the maximum number of reference points. Within this sector smaller (sub-) 15° central, 15° west, and 30° east sectors were delimited (Fig. 4a).

It is important to point out that, when delimiting the sectors, several sampling sites in the zone close to the accident epicenter, both to the east and to the west, appeared to be outside of the modeled area. At the same time, the area was significantly expanded due to the unsampled locations at the remote north-east border. For this reason another model was suggested, aiming to divide the study area into rectangles (Fig. 4b). The created contamination maps (see Fig. 3) provide well described, narrow, central and west rectangles (each 4 km wide), and a broader east rectangle (7 km wide). All of the points were attributed to either the central, west, or east part depending on the model employed.

For each model area, the dependencies of soil contents for <sup>90</sup>Sr, <sup>137</sup>Cs, and <sup>239,240</sup>Pu ( $y(x)$ , kBq m<sup>-2</sup>) on the distance ( $x$ , km) to the epicenter were assessed at corresponding attributed points. The calculation of the  $x$  value (km) varied depending on the model

**Table 8**

Coefficients of variation (CV) for the distribution of radionuclide content at the limited EURT areas, %.

Sampling location	<sup>90</sup> Sr	<sup>137</sup> Cs	<sup>239,240</sup> Pu
Trace axis	36.1	28.1	36.4
West peripheral area	32.3	9.3	17.2
East peripheral area	68.9	13.4	10.6

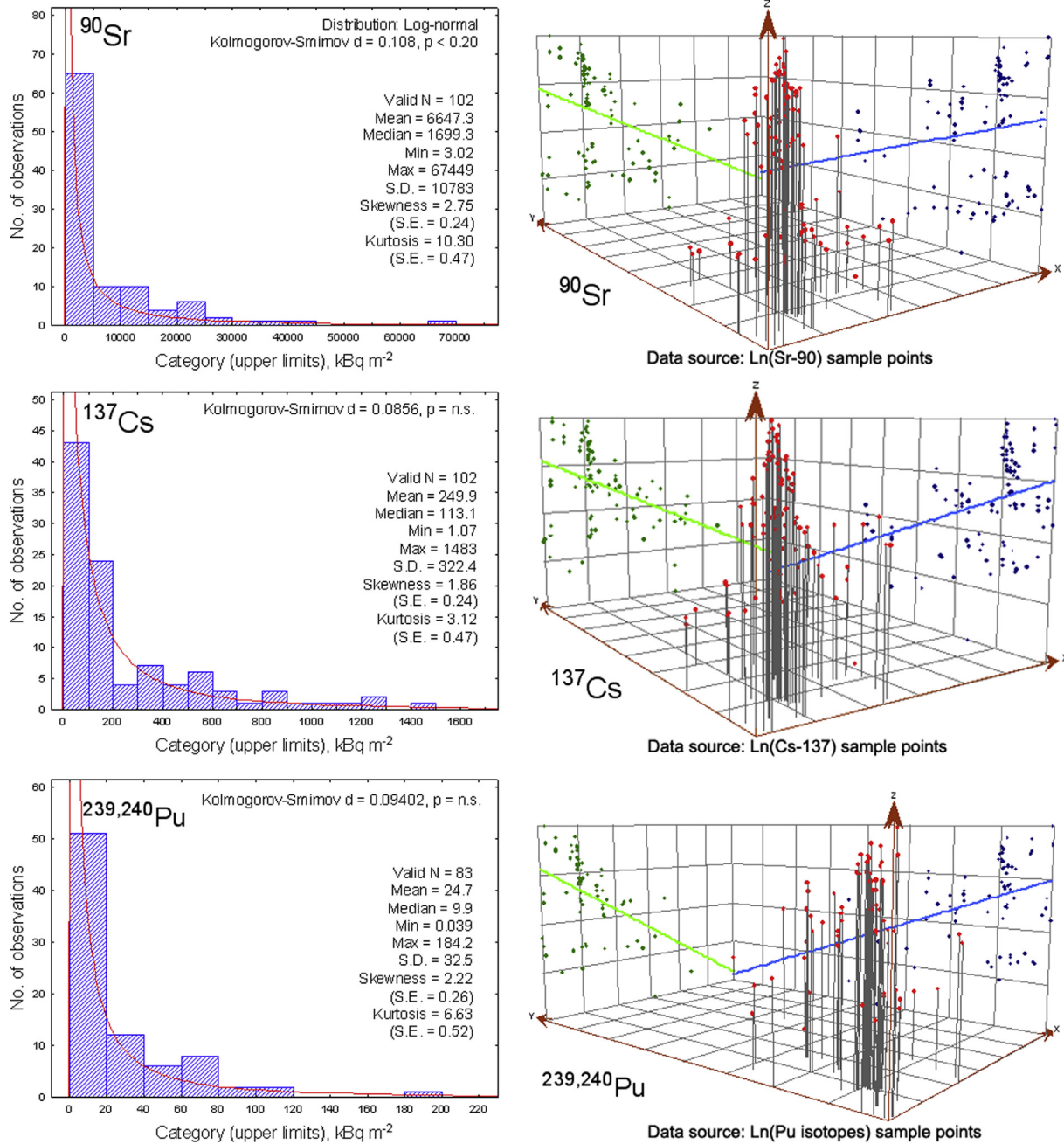


**Fig. 2.** Empirical (sample) distributions of radionuclide density contamination ( $\text{kBq m}^{-2}$ ) with its log-normal approximation (left column) and linear trends for logarithmic data (right column).

type. When sector delimitation was applied, the model used the Euclidian distance between the points and epicenter (along the radius). In the case of rectangular delimitation, the  $x$  value was the length of the projection of the same metric on the trace axis along

**Table 9**  
 Ordinary kriging parameters (exponential variogram models) for the transformed data of  $^{90}\text{Sr}$ ,  $^{137}\text{Cs}$ ,  $^{239,240}\text{Pu}$  contamination density.

Parameter	$^{90}\text{Sr}$	$^{137}\text{Cs}$	$^{239,240}\text{Pu}$
Nugget, $C_0$ , ( $\text{kBq m}^{-2}$ ) <sup>2</sup>	2.5118	0.8036	1.6465
Partial sill, $C_1$ , ( $\text{kBq m}^{-2}$ ) <sup>2</sup>	2.8532	1.0060	0.9097
Nugget-to-sill, $C_0/(C_0 + C_1)$ , %	47	44	64
Major range, $R_1$ , km	6.497	14.832	39.805
Minor range, $R_2$ , km	3.687	6.154	6.387
Direction, degree	26.4	21.6	17.5
Anisotropy factor, $R_1/R_2$	1.76	2.41	6.23

which the rectangles were aligned. As a criterion for choosing the appropriate type of function  $y(x)$ , we used  $R^2$  determination coefficient defining the proportion of initial data variation explained by the best-fit line (i.e. approximation quality in whole). The analysis of different types of functions via  $R^2$  showed that all the areas are best approximated by the following exponential equation:  $y(x) = e^{(b_0 + b_1 \cdot x)}$ , where  $b_0$  and  $b_1$  are linear regression coefficients for the variable  $\text{Ln}\{y(x)\}$ . The estimated parameters, their standard errors and the  $R^2$  coefficients are presented in Table 10. Since radionuclide contamination density in close proximity has a high level of variability, the  $R^2$  values in some cases are not very high, revealing the low prediction performance of the approximation. Nevertheless, they are still the most significant among  $R^2$  for the other approximation equations analyzed in this work.

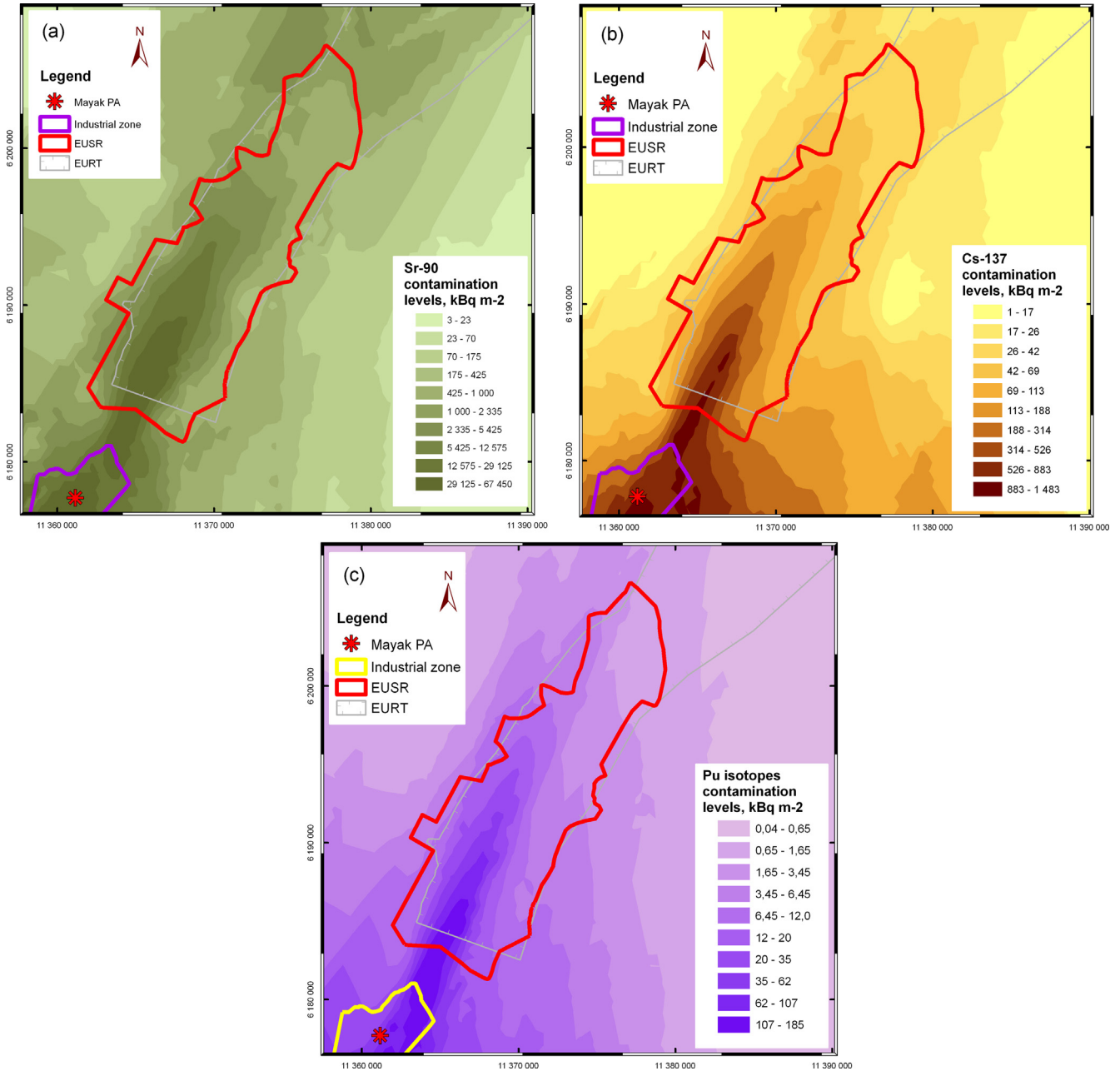


Fig. 3. Ordinary kriging type estimated prediction maps of radionuclide content in the EURT soil (kBq m<sup>-2</sup>): a) <sup>90</sup>Sr, b) <sup>137</sup>Cs, c) <sup>239,240</sup>Pu.

Using the empirically established parameters for the spatial distribution functions  $y(x)$  of soil contamination density, the integrated quantities of radionuclides ( $I$ ) in the 4–35 km distance interval were calculated as follows:

- for a sector with the angle  $\varphi$ (deg.) – with an iterated integral in the polar coordinates:

$$I = 2\pi \times \frac{\varphi}{360} \times 10^{-3} \times \int_4^{35} x \cdot e^{(b_0+b_1 \cdot x)} dx, \text{ TBq}$$

- for a  $w$  km-wide rectangle – with a simple integral in the Cartesian coordinates:

$$I = w \times 10^{-3} \times \int_4^{35} e^{(b_0+b_1 \cdot x)} dx, \text{ TBq}$$

The results of the integrated assessment of radionuclide contents and corresponding uncertainty values for all the model areas of the study territory are presented in Table 11. The Monte Carlo method was applied to get a quantitative assessment of uncertainties determined by the statistical errors for an approximation of the raw measurement data (i.e. errors of coefficients  $b_0$  and  $b_1$ ). To this end, random  $I$  values were modeled from the above formulas using the coefficients  $b_0$  and  $b_1$  generated in accordance with normal distribution (for each case 10,000 values were generated).  $I$  values are asymmetrically (log-normally) distributed. The median of the distribution is approximately equal to the point estimation obtained for the initially calculated  $b_0$  and  $b_1$ . It is

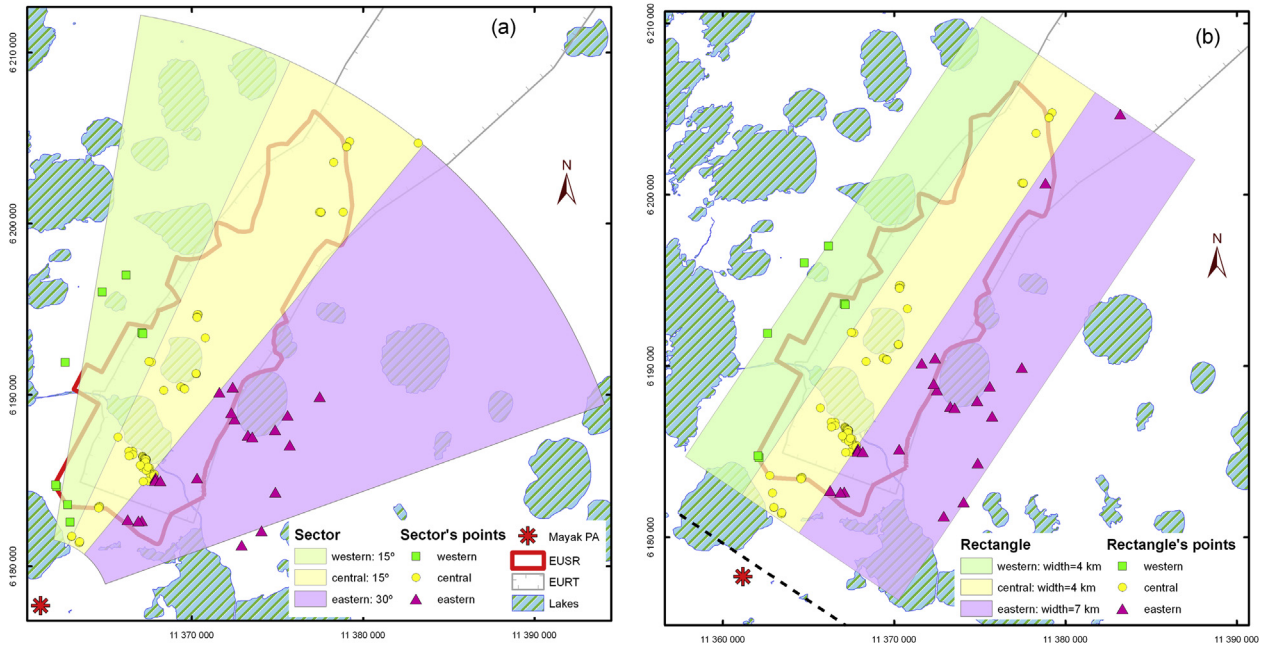


Fig. 4. Positioning of the reference points within the model areas – sectors (a) and rectangles (b).

Table 10 Regression parameters, standard error values, and R<sup>2</sup> determination coefficients calculated with the different models.

Sectors model									
Parameter	Central ( $\varphi = 15$ deg)			West ( $\varphi = 15$ deg)			East ( $\varphi = 30$ deg)		
	<sup>90</sup> Sr	<sup>137</sup> Cs	<sup>239,240</sup> Pu	<sup>90</sup> Sr	<sup>137</sup> Cs	<sup>239,240</sup> Pu	<sup>90</sup> Sr	<sup>137</sup> Cs	<sup>239,240</sup> Pu
Area, km <sup>2</sup>	158.26			158.26			316.52		
$b_0 \pm$ st.er.	10.3 ± 0.4	6.9 ± 0.2	4.8 ± 0.4	4.7 ± 0.4	3.4 ± 0.3	0.14 ± 0.65	6.3 ± 0.6	6.4 ± 0.7	0.19 ± 0.20
$b_1 \pm$ st.er.	-0.16 ± 0.02	-0.12 ± 0.02	-0.18 ± 0.03	-0.10 ± 0.03	-0.07 ± 0.02	-0.03 ± 0.05	-0.18 ± 0.04	-0.20 ± 0.05	-0.04 ± 0.02
R <sup>2</sup>	0.39	0.50	0.43	0.67	0.57	0.16	0.47	0.47	0.61
Rectangles model									
Parameter	Central (w = 4 km)			West (w = 4 km)			East (w = 7 km)		
	<sup>90</sup> Sr	<sup>137</sup> Cs	<sup>239,240</sup> Pu	<sup>90</sup> Sr	<sup>137</sup> Cs	<sup>239,240</sup> Pu	<sup>90</sup> Sr	<sup>137</sup> Cs	<sup>239,240</sup> Pu
Area, km <sup>2</sup>	124.00			124.00			217.00		
$b_0 \pm$ st.er.	9.9 ± 0.4	6.6 ± 0.3	4.3 ± 0.4	4.4 ± 0.6	3.1 ± 0.6	2.4 ± 2.9	6.2 ± 0.6	5.0 ± 0.5	0.6 ± 0.1
$b_1 \pm$ st.er.	-0.14 ± 0.03	-0.11 ± 0.02	-0.14 ± 0.03	-0.09 ± 0.04	-0.06 ± 0.04	-0.17 ± 0.18	-0.18 ± 0.05	-0.10 ± 0.03	-0.08 ± 0.01
R <sup>2</sup>	0.24	0.33	0.24	0.50	0.32	0.48	0.46	0.32	0.96

Table 11 Radionuclide content within boundaries of the model sectors and rectangles within the head part of the EURT.

Sectors model									
Parameter	Central ( $\varphi = 15$ deg)			West ( $\varphi = 15$ deg)			East ( $\varphi = 30$ deg)		
	<sup>90</sup> Sr	<sup>137</sup> Cs	<sup>239,240</sup> Pu	<sup>90</sup> Sr	<sup>137</sup> Cs	<sup>239,240</sup> Pu	<sup>90</sup> Sr	<sup>137</sup> Cs	<sup>239,240</sup> Pu
Area, km <sup>2</sup>	158.26			158.26			316.52		
Content, TBq	253.638	13.858	0.857	2.241	0.971	0.085	7.517	6.274	0.144
Upper bound	585.978	24.265	1.896	6.280	2.545	0.668	31.762	30.997	0.273
Lower bound	113.989	8.214	0.403	0.888	0.412	0.014	2.087	1.488	0.078
Rectangles model									
Parameter	Central (w = 4 km)			West (w = 4 km)			East (w = 7 km)		
	<sup>90</sup> Sr	<sup>137</sup> Cs	<sup>239,240</sup> Pu	<sup>90</sup> Sr	<sup>137</sup> Cs	<sup>239,240</sup> Pu	<sup>90</sup> Sr	<sup>137</sup> Cs	<sup>239,240</sup> Pu
Area, km <sup>2</sup>	124.00			124.00			217.00		
Content, TBq	316.656	16.631	1.152	2.438	0.964	0.130	9.275	7.030	0.102
Upper bound	810.954	30.439	2.837	9.753	4.045	155.911	33.881	20.588	0.131
Lower bound	133.290	9.476	0.509	0.740	0.280	0.001	2.773	2.616	0.080

reasonable to determine the reliability of point estimation through the asymmetric (to the median) 95% confidence interval equal to the 5th (lower bound) and 95th (upper bound) percentiles of the modeled distribution of random  $I$  values. Given the insignificant distribution asymmetry, the uncertainty corresponds to the  $2 \times$  S.D. range (see Table 11).

Integrated quantities calculated with the sector- and rectangle-shaped models are similar. For instance, within the west peripheral area, they are in good agreement for  $^{90}\text{Sr}$  and  $^{137}\text{Cs}$ . The model employing rectangles yields the integrated quantities of somewhat higher within the central axis of the trace and the east peripheral area. However, when considering the uncertainty bounds, these differences are statistically insignificant.

#### 4. Discussion

As demonstrated earlier, the soils within the EURT central axis have a concentration of the principal amount of  $^{90}\text{Sr}$  (75%) and  $^{239,240}\text{Pu}$  (70%). At the same time most of the  $^{137}\text{Cs}$  (77%) is located in the west and east parts of the trace, contaminated by the Karachay accident in 1967. When moving further away from the accident epicenter the changes in radionuclide content were approximated by the exponential function with a high degree of certainty (Molchanova et al., 2009). The newly obtained data fits very well into the course of the exponential function suggested earlier. The functions provide a more detailed view of the spatial distribution of radionuclides in the head part of the EURT. The radionuclide quantities in the trace peripheral areas were not previously assessed. In this paper the boundaries of the study area were pushed west and east from the central axis to the point of transition of the contamination gradient to the background level values. The study area was clearly split into 3 parts – central, west, and east. For all areas the activity of radionuclides ranges as  $^{90}\text{Sr} > ^{137}\text{Cs} > ^{239,240}\text{Pu}$ . The radionuclide content values are highest within the central part of the trace and drop about hundred times down when moving west or east from the central axis. The radionuclide contents in soils of the west peripheral area are 2–5 times lower than those in soils of the east one. Mapping of the data clearly illustrates the spatial distribution of the contamination density of  $^{90}\text{Sr}$ ,  $^{137}\text{Cs}$ , and  $^{239,240}\text{Pu}$  within the study area.

The complex nature of the formation of the contaminated area and the initial asymmetry of contamination was mostly determined by weather conditions, particularly by the wind direction at the times of the incidents (1957 and 1967) (Teterin, 2011). Spatial redistribution of radionuclides has been occurring since the accidents. This has been due to natural causes: namely isotopes' migration capacities; physical geographic environmental conditions; terrain relief; prevailing easterly and north-easterly winds and the water runoff vectors (Chukanov et al., 1996; Cigna et al., 2000; Sokolov and Krivolutsky, 1993). The redistribution processes were also affected by the soil types, characteristics of the vegetation in the biogeocenoses, and frequent fires. Moreover, most of the area underwent recultivation efforts that also impacted on radionuclide redistribution. Even at locations close to each other these factors resulted in contamination densities that may differ by up to a factor of ten.

Finally, the currently existing shape of the trace was formed due to many factors. No noticeable redistribution of radionuclide content was detected over the course of the research program which lasted over 2003–2012. Therefore, the parameters monitored were varying over the average values. This suggests that the spatial redistribution over 2003–2012 can be neglected because the initial contamination levels were already quite diverse.

The contamination pattern is still being formed by the still ongoing scheduled emissions from the PA Mayak facilities. These aerosol fallouts follow the prevailing north-easterly and easterly winds that result in additional contamination of the east section of the trace (Bakurov et al., 2007).

The values for integrated quantities were calculated using the sector- and rectangle-shaped geometric models. In some cases, the calculations demonstrated very good agreement. While in others, elevation in radionuclide quantity was observed. This is due to the fact that the area next to the accident epicenter was broader and included more sampling locations when using the rectangles model, while using the sectors model, a smaller area with low contamination levels and a lower number of sampling points were included in calculations. In both cases, however, the integrated content for all of the radionuclides remain within the uncertainty limits calculated by the Monte Carlo method.

#### 5. Conclusion

- i. In this paper the database on radionuclide contamination of the EURT within 0–35 km from the epicenter of the Kyshtym accident has been analyzed. As a result, prediction maps of the contamination density for  $^{90}\text{Sr}$ ,  $^{137}\text{Cs}$ , and  $^{239,240}\text{Pu}$  in the head part of the trace were created.
- ii. Integral contents of  $^{90}\text{Sr}$ ,  $^{137}\text{Cs}$ , and  $^{239,240}\text{Pu}$  were calculated using two types of geometrical models. The results obtained using these models are in good agreement. However, applying the rectangle-shaped model leads to some slight overestimation of radionuclide content due to its dealing with a bigger area situated near the epicenter.
- iii. The spatial distribution pattern of radionuclides obtained in this work can be further used when performing monitoring in areas near the PA Mayak nuclear facilities as well as when assessing results for secondary transitions of radionuclides originated from emergency situations (fires, tornados, wind blows-off, etc.).
- iv. The research will be continued in order to estimate radionuclide contents in different components of ecosystems as well as for the calculation of doses absorbed by non-human biota. An analysis of all the data will provide a comprehensive view of the radioecology of the terrestrial ecosystems in the EURT and adjacent areas.

#### Acknowledgments

This work was done with financial support from the Program for the multidisciplinary researches between Institutes of UB RAS (project No 12-M-24-2016), and the Federal Special Scientific & Technical Program in support of leading scientific schools (SS-2840.2014.4). We are indebted to M. Krivinuyk (Turianski & Wolfsson Company), Dr. K. Ivanovskikh (Ural Federal University) and M.H. Lyman for linguistic advice, and Dr. A. Sergeev (IIE UB RAS) for expert recommendations on the geostatistical modeling. Helpful remarks of two anonymous reviewers and JER Associate Editor, J.R. Twining are gratefully acknowledged.

#### References

- Aarkrog, A., Dahlgaard, H., Nielsen, S.P., Trapeznikov, A.V., Molchanova, I.V., Pozolotina, V.N., Karavaeva, E.N., Yushkov, P.I., Polikarpov, G.G., 1997. Radioactive inventories from the Kyshtym and Karachay accidents: estimates based on soil samples collected in the South Urals (1990–1995). *Sci. Total Environ.* 201, 137–154.
- Aarkrog, A., Dalgaard, H., Nielsen, S.P., Pozolotina, V.N., Molchanova, I.V., Karavaeva, E.N., Yushkov, P.Y., Trapeznikov, A.V., 1998. Study on the contribution of major nuclear incidents to radioactive contamination of the Ural region. *Russ. J. Ecol.* 29, 31–37.

- Bakurov, A.S., Shejn, G.P., Aksenov, G.M., Rovny, S.I., 2007. The Use of "Ural Experience" in the Development of Emergency Measures for the Rehabilitation of Fishery Reservoirs at the Chernobyl Accident Zone, the Experience of Overcoming the Consequences of Industrial Accidents and the Development of Nuclear Technology, Chelyabinsk, Russia, pp. 8–25.
- Brown, J.E., Alfonso, B., Avila, R., Beresford, N.A., Copplestone, D., Prohl, G., Ulanovsky, A., 2008. The ERICA tool. *J. Environ. Radioact.* 99, 1371–1383.
- Caro, A., Legarda, F., Romero, L., Herranz, M., Barrera, M., Valiño, F., Idoeta, R., Olondo, C., 2013. Map on predicted deposition of Cs-137 in Spanish soils from geostatistical analyses. *J. Environ. Radioact.* 115, 53–59.
- Chen, Q., Aarkrog, A., Nielsen, S.P., Dahlgaard, H., Nies, H., Yixua, Y., Mandrup, K., 1993. Determination of plutonium in environmental samples by controlled valence in anion exchange. *J. Radioanal. Nucl. Chem.* 172, 281–288.
- Chukanov, V.N., Bazhenov, A.V., Varaksin, A.N., et al., 1996. The East Ural Radioactive Trace (Sverdlovsk Region). UB RAN, Ekaterinburg.
- Cigna, A.A., Romero, L., Monte, L., Karavaeva, Y.N., Molchanova, I.V., Trapeznikov, A., 2000. <sup>90</sup>Sr profile in soil samples from the East Urals Radioactive Trail (EURT): a quantitative approach. *J. Environ. Radioact.* 49, 85–96.
- Dubois, G., Bossew, P., 2003. Chernobyl <sup>137</sup>Cs deposition in Austria: analysis of the spatial correlation of the deposition levels. *J. Environ. Radioact.* 65, 29–45.
- ESRI ArcGIS. Environmental Systems Resource Institute, 2009, Redlands.
- Facchinelli, A., Sacchi, E., Mallen, L., 2001. Multivariate statistical and GIS-based approach to identify heavy metal sources in soils. *Environ. Pollut.* 114 (3), 313–324.
- Grubich, A., Makarevich, V.I., Zhukova, O.M., 2013. Description of spatial patterns of radionuclide deposition by lognormal distribution and hot spots. *J. Environ. Radioact.* 126, 264–272.
- Hammersley, J.M., Handscomb, D.C., 1964. Monte Carlo Methods. Methuen, London.
- Hejl, A.M., Ottmar, R.D., Jannik, G.T., Eddy, T.P., Rathbun, S.L., Commodore, A.A., Pearce, J.L., Naeher, L.P., 2013. Radionuclide activity concentrations in forest surface fuels at the Savannah River site. *J. Environ. Manag.* 115, 217–226.
- ISO/IEC 17025, 2005. General Requirements for the Competence of Testing and Calibration Laboratories. ISO, Geneva, Switzerland.
- Johnston, K., Ver Hoef, J.M., Krivoruchko, K., Lucas, N., 2001. Using ArcGIS Geostatistical Analyst. ESRI, Redlands.
- Karimullina, E., Antonova, E., Pozolotina, V., 2013. Assessing radiation exposure of herbaceous plant species at the East-Ural Radioactive Trace. *J. Environ. Radioact.* 124, 113–120.
- Laverov, N.P., 2007. Atlas of Geological and Ecological Maps for the Observation Area of the PA Mayak. Geospeceecologia, Moscow-Ozyorsk.
- Mabit, L., Bernard, C., 2007. Assessment of spatial distribution of fallout radionuclides through geostatistics concept. *J. Environ. Radioact.* 97 (2–3), 206–219.
- Mikhailovskaia, L.N., Molchanova, I.V., Karavaeva, E.N., Pozolotina, V.N., Tarasov, O.V., 2011. Radioecological investigation of the soil cover of eastern Urals State radioactive reserve and neighboring areas. *Radiats Biol. Radioecol.* 51, 476–482.
- Molchanova, I.V., Pozolotina, V.N., Karavaeva, E.N., Mikhaylovskaya, L.N., Antonova, E.V., Antonov, K.L., 2009. Radioactive inventories within the East-Ural radioactive state reserve on the Southern Urals. *Radioprotection* 44, 747–757.
- Pozolotina, V.N., Molchanova, I.V., Karavaeva, E.N., Mikhaylovskaya, L.N., Antonova, E.V., 2008. The Current State of Terrestrial Ecosystems at the East Ural Radioactive Trace Area: Contamination Levels and Biological Effects. Goschitsky Press, Ekaterinburg.
- Pozolotina, V.N., Molchanova, I.V., Mikhaylovskaya, L.N., Antonova, E.V., Karavaeva, E.N., 2012. The current state of terrestrial ecosystems in the Eastern Ural Radioactive Trace. In: Gerada, J.G. (Ed.), Radionuclides: Sources, Properties and Hazards. Nova Science, New York, pp. 1–22.
- Raputa, V.F., 2006. Models for the reconstruction of the axis part of the East Ural Radioactive Trace. *Comput. Technol.* 11, 10–16.
- Romanov, G.N., Nikipelov, B.V., Drozhko, E.G., 1990. The Kyshtym Accident: Causes, Scale and Radiation Characteristics, Seminar on Comparative Assessment of the Environmental Impact of Radionuclides Released during Three Major Nuclear Accidents: Kyshtym, Windscale, Chernobyl. Commission of the European Communities, Luxembourg, pp. 25–40.
- Rubinstein, R.Y., Kroese, D.P., 2008. Simulation and the Monte Carlo Methods. John Wiley & Sons, Inc., New Jersey.
- Sokolov, V.E., Krivolutsky, D.A., 1993. Ecological After-effects of the Radioactive Contamination at South Urals. Nauka, Moscow.
- Teterin, A.F., 2011. Ecological and Climatic Characteristics at the East Ural Radioactive Trace Area. UB RAN, Ekaterinburg.
- Tsaturov, Y.S., Anisimova, L.I., 1993. Radionuclide Contaminated Territories of Russia: Identification, Restoring and Rehabilitation Aspects, Remediation and Restoration of Radioactive-contaminated Sites in Europe, Antwerpen, pp. 309–324.
- Tsvetaeva, N.E., Filin, V.M., Ivanova, L.A., Revnov, V.N., Rodionov, E.P., Rudaya, L.Y., Suslin, I.A., Shapiro, K.Y., 1984. Use of mono isooctylmethylphosphonic acid and its trivalent iron salt in determining radionuclides in effluents. *Sov. At. Energy* 57, 548–552.
- Van der Perk, M., Lev, T., Gillett, A.G., Absalom, J.P., Burrough, P.A., Crout, N.M.J., Garger, E.K., Semiochkina, N., Stephanishin, Y.V., Voigt, G., 2000. Spatial modelling of transfer of long-lived radionuclides from soil to agricultural products in the Chernigov region, Ukraine. *Ecol. Model.* 128, 35–50.
- Vasilenko, V.N., Kyamkin, A.M., et al., 1998. Cartography of Sr-90, Cs-137 and Pu Isotopes Integrated Contamination in Urals within Chelyabinsk, Sverdlovsk and Kurgan Regions on Scale 1:200 000 in 1997 and 1957 yy. IGKE of Rosgidromet and RAS, Moscow.
- Volobuev, P.V., Chukanov, V.N., Shtinov, N.A., Alekseenko, N.N., 2004. Technogenic radioactive accidents in Urals, estimations and accuracy. In: Chukanov, V.N. (Ed.), Urals. Radiation. Rehabilitation. UB RAS, Ekaterinburg, pp. 10–49.
- Webster, R., Oliver, M.A., 2007. Geostatistics for Environmental Scientists. John Wiley and Sons Ltd., Chichester.
- Yatsalo, B.I., Balonov, M.I., Golikov, V.Yu., Didenko, V.I., 2000. Application of GIS for population dose assessment in the Chernobyl accident area. In: 10th International Congress of the International Radiation Protection Association, Hiroshima, Japan.
- Zhao, Y., Yan, D., Zhang, Q., Zhan, J., Hu, H., 2012. Spatial distributions of <sup>137</sup>Cs in surface soil in Jing-Jin-Ji Region, North China. *J. Environ. Radioact.* 113, 1–7.